An efficient and robust procedure to calculate absorption spectra of aqueous charged species applied to NO_2^-

Lina Uribe,[†] Sara Gómez,[*,‡] Tommaso Giovannini,[‡] Franco Egidi,[‡] and Albeiro Restrepo[*,†]

†*Instituto de Química, Universidad de Antioquia UdeA, Calle 70 No. 52-21, Medellín, Colombia*

‡*Scuola Normale Superiore, Classe di Scienze, Piazza dei Cavalieri 7, 56126, Pisa, Italy*

E-mail: sara.gomezmaya@sns.it; albeiro.restrepo@udea.edu.co

1

Abstract

Accurate calculation of absorption spectra of aqueous NO_2^- requires rigorously sampling the quantum potential energy surfaces for microsolvation of NO_2^- with at least five explicit water molecules and embedding the resulting clusters in a continuum solvent accounting for the statistical weighted contributions of individual isomers. This method, which we address as ASCEC + PCM, introduces several desired features when compared against MD simulations derived QM/MM spectra: comparatively fewer explicit solvent molecules to be treated with expensive QM methods, the identification of equilibrium structures in the quantum PES to be used in further vibrational spectroscopy, and the unequivocal identification of cluster orbitals undergoing electronic transitions and charge transfer that originate the spectral bands.

1 Introduction

The problem of correctly modeling the spectroscopic properties of molecules in aqueous solution is of fundamental importance in many fields of chemistry due to the ubiquity of water as a solvent as well as to the advantages offered by the ability to both correctly predict and interpret experimental measurements, which can only be unlocked through the use of suitably reliable and cost effective computational models.[1–9] Therefore, much effort has been devoted to the development of computational methods for the treatment of solvation, in parallel with the search for new electronic structure models and their extension to the calculation of molecular properties as well as energies. This considerable effort has resulted in many different classes of methods, each with their own merits and drawbacks. One way to classify solvation approaches is through the choice of method for the treatment of the solvent itself, since the solute must always be treated quantum mechanically in order to simulate spectroscopic properties. Therefore, one can resort to either classical,[1,10–19] quantum,[2,20–26] or mixed classical/quantum[27–31] methods, as well as adaptive QM/MM methodologies,[32–34] for the treatment of the solvent, with the goal of including all relevant solute···water interactions at an amenable computational cost.[4] An additional issue that must be tackled is the fact that a solution is a dynamical system where the microsolvated environment of the solute cannot be represented by means of a single solvent configuration, and is rather an ensemble of many different structures. The correct simulation of any solute spectroscopic properties should be based upon a proper sampling of the solute···solvent configurational landscape.[35] For this purpose one may opt for a explicit sampling by means of a classical molecular dynamcis (MD) simulation, from which a sufficient number of structures, also known as "snapshots", can be extracted, and the final spectrum is obtained by adding up the spectra from each snapshot.[4] Another type of approach may be based on the careful selection of a limited number of minimum energy solute···solvent "clusters", and the final spectrum is then the free energy weighted average of the spectra computed from each of the clusters.[36] It

should be clear from this very brief discussion that the choice of solvation methods is indeed quite vast, and the panoply of available options notwithstanding, there is a lack of systematic studies carefully comparing the performances of methods based on different paradigms. In this work, we attempt to add to this discussion by comparing two very different types of state of the art approaches for the simulation of electronic absorption spectra: a cluster based method, and MD based polarizable QM/MM methods.[4] In addition to the spectral simulations, we offer a comprehensive picture of structural aspects, energies and bonding, and their effects on the UV–Vis absorption spectrum, which we compute over structures obtained from both structural samplings using polarizable continuum models[3,37–42] (PCM), and hybrid polarizable quantum mechanics/molecular mechanics (QM/MM) methods,[15] based on Fluctuating Charges (FQ) or Fluctuating Charges and Dipoles (FQFμ).[4,10,43–47]

In order to systematically explore the performances of the two approaches we select the nitrite ion, NO_2^-, as a case of study. This small inorganic molecule allows for a wide testing of the methodologies thanks to the reduced computational cost, and is ideal for the purpose of comparing absorption spectra thanks to its easily assigned electronic transition. Nonetheless, being an inorganic anion, this small systems still represents a challenge because it has a diffuse electronic density whose interaction with the solvent environment can be arduous to model.[48]

Due to is noxious impact in human health, NO_2^- content is regularly monitored in groundwater, wastewater, and water treatment plants by chromatography,[49] electrochemistry[50] and spectroscopy techniques.[51–62] Fittingly, the US Environmental Protection Agency (EPA) has set a maximum nitrite level of 1.0 mg L^{-1} in drinking water,[63] while the European Union limits are one order of magnitude lower.[64] Since nitrites in food and drinks play an important role in human health, experimental protocols for their detection and accurate quantification are highly desirable, nonetheless, present day techniques to characterize NO_2^- in solution

4

require complicated procedures.[65] Several spectroscopic procedures are available to analyze nitrites in aqueous solution using among others UV–Vis,[52,53] and Raman.[55] Although NO_2^- can be directly detected with UV–Vis, the spectral signals overlap with those of NO_3^-,[55,66] thus, a protocol for indirect detection of NO_2^- is regularly used, which requires that samples be processed via the Griess reaction, there, the solution suspected of containing nitrites is treated with sulfanilic acid and naphthyl–1–amine in acidic medium, leading to the formation of a deeply colored red azo dye.

2 Methods

2.1 The structural problem

Sampling of the complex energy landscapes involved in the microsolvation of charged species is a multilevel hard problem:[67] there is the exponential growth of the number of local minima that usually populate small energy windows within the corresponding global minimum, there is the weak nature of the intermolecular interactions, and there is the problem of how to accurately treat solvent effects. Here, we tackle the structural problem in two alternative manners:

1. The B3LYP/6–311++G(d, p) optimized geometry of NO_2^- was used to generate the electrostatic potential needed to construct the GAFF[68] force field to be used in molecular dynamics simulations. Then, NO_2^- was placed at the center of a cubic box, setting the distances to the walls to 2.0 nm, and filling the available space with 4625 TIP3P[69] water molecules. One water molecule was randomly replaced with a Na^+ counterion. Then, we used GROMACS 2020.3[70] to run duplicate 30 ns MD simulations under the conditions[68–76] summarized in Table S1 in the electronic supplementary material. Equilibration occurred during the first few nanoseconds, thus, to guarantee represen-

tative microstates of the equilibrated system, we took 200 snapshots during the final 20 ns of the trajectories and proceeded to calculate absorption spectra. Hydration patterns were extracted using the TRAVIS package.[77,78]

2. We undertook systematic stochastic searches of the potential energy surfaces of the $[NO_2 (H_2O)_x]^-$ clusters with $x = 1 - 6$. We used a simulated annealing procedure[79,80] which contains a modified Metropolis test and quantum interaction energies, as implemented in the ASCEC (ASCEC stands for the Spanish acronym Annealing Simulado Con Energía Cuántica) algorithm.[81–83]

Brief description of ASCEC: The algorithm explores complex energy landscapes by undertaking random walks of the corresponding configurational space. To completely avoid structural bias, in our method, we start from the worst possible configuration, in which the charged species and all solvent molecules are superimposed at the center of a cubic box (we call this the initial big bang conditions). Following the original algorithm developed by Metropolis et al.,[79] this cubic box defines the physical space available for the evolution of the system under the annealing conditions. ASCEC calls an external program (Gaussian16[84] in this particular work) to calculate the quantum energy of every randomly generated structure, which is then the subject of a modified Metropolis acceptance test as follows: as usual, random structural changes that result in lower energy conformations ($\Delta E < 0$) are accepted. However, if $\Delta E > 0$, the new structure is accepted if $\Phi(\Delta E) < P(\Delta E)$, where $P(\Delta E) = \exp(-\Delta E/k_B T)$ is the temperature–dependent Boltzmann probability distribution function and $\Phi(\Delta E)$ = $|\Delta E/E_j|$, j being the structure under evaluation. This criterion is more adequate than the usual procedure of comparing $P(\Delta E)$ to a randomly generated number in the [0, 1] interval because under the latter, good structures may be randomly rejected and bad structures may be randomly accepted.[82,83] If neither test is satisfied, the move is not accepted and the structure that originated the change is randomly modified again.

6

Since only the accepted structures are changed, this procedure effectively amounts to constructing a Markov chain of points in the configurational space.

A typical run of ASCEC requires the following information (See Table S2 in the electronic supplementary material for the specific annealing conditions): (i) a quenching route (ii) the initial geometry in Cartesian coordinates (iii) the geometry of the box (iv) the maximum initial number of structures to be evaluated before going to the next temperature (v) the maximum allowed atom displacements, and (vi) a combination of Hamiltonian or functional and basis set for energy calculations. Final equilibrium structures after multiple ASCEC runs and further optimization and characterization of the candidate structures for each molecularity are reported at the B3LYP/6–311++G(d, p) level. Binding energies are calculated as the difference between the energy of a particular cluster and the energies of the isolated components, in this way, negative binding energies represent stabilizing interactions. The Counterpoise method[85] was used to correct for the basis set superposition error. Highly accurate interaction energies on the DFT optimized clusters were calculated via the sophisticated DLPNO–CCSD(T) method[86,87] as implemented in the 4.2.1 version of ORCA.[88] All optimization and frequency calculations were carried out using the Gaussian16 suite of programs.[84]

2.2 Dissection of bonding interactions

To accurately describe the delicate interactions that keep the clusters representing microsolvated states of NO_2^- as stable units is a complex theoretical problem. In this work, we use the tools provided by the Natural Bond Orbitals (NBO[89–91]) and by the Quantum Theory of Atoms In Molecules (QTAIM[92–96]). These are both well established analysis procedures firmly rooted in quantum mechanics, which we use here to draw insight into the nature of bonding interactions from the explicit microsolvated structures produced by the stochastic search in the following ways:

1. A number of QTAIM descriptors of the nature of intermolecular interactions are available after analysis of the topology of a given electron distribution. In particular, we derive insight from the properties of bond critical points (BCPs, $\mathbf{r}_c$) of the electron density, which are local extrema $\left(\vec{\nabla}\rho\left(\mathbf{r}_c\right) = 0\right)$ with two negative and one positive curvatures in a given bond path linking two atoms. In short, local properties of the electron density at BCPs are related to the nature of the intermolecular interactions in the following way:[97–99]

    (a) $\nabla^2\rho\left(\mathbf{r}_c\right) > 0$ characterizes a local minimum in the electron density at $\mathbf{r}_c$, indicating long range, weak interactions. $\nabla^2\rho\left(\mathbf{r}_c\right) < 0$ characterizes local maxima in the electron density at $\mathbf{r}_c$, describing increasingly covalent interactions

    (b) Accumulation of electron density: larger $\rho\left(\mathbf{r}_c\right)$ is indicative of stronger, increasingly covalent interactions

    (c) Local kinetic energy densities $\mathcal{G}\left(\mathbf{r}_c\right)/\rho\left(\mathbf{r}_c\right)$ are everywhere positive and repulsive while local potential energy densities $\mathcal{V}\left(\mathbf{r}_c\right)/\rho\left(\mathbf{r}_c\right)$ are everywhere negative and attractive. Accordingly, the sign of the total energy density $\mathcal{H}\left(\mathbf{r}_c\right)/\rho\left(\mathbf{r}_c\right) = \mathcal{G}\left(\mathbf{r}_c\right)/\rho\left(\mathbf{r}_c\right) + \mathcal{V}\left(\mathbf{r}_c\right)/\rho\left(\mathbf{r}_c\right)$ reveals the local imbalance between the two terms and therefore leads to $\mathcal{H}\left(\mathbf{r}_c\right)/\rho\left(\mathbf{r}_c\right) > 0$ representing locally repulsive regions for the electron interaction, which are associated to long range, weak interactions, and to $\mathcal{H}\left(\mathbf{r}_c\right)/\rho\left(\mathbf{r}_c\right) < 0$ representing locally attractive regions for the electron interaction, which are associated to increasingly stronger interactions. The same picture is afforded by a dimensional analysis: energy densities have the same units as pressure, thus, locally positive total electron energies (positive pressures) push electrons away from the BCP, towards the nuclei, describing long range interactions, while locally negative total electron densities (negative pressures) describe covalent bonds by virtue of sucking electrons from both nuclei towards the shared BCP region. The total energy density for a given critical point, $\mathcal{H}\left(\mathbf{r}_c\right)/\rho\left(\mathbf{r}_c\right)$, is often addressed as the bond degree parameter[100]

(d) The local virial ratio offers a quantitative classification of intermolecular interactions according to[97,100] $|\mathcal{V}(\mathbf{r}_c)|/\mathcal{G}(\mathbf{r}_c) > 2 \Rightarrow$ covalent, $|\mathcal{V}(\mathbf{r}_c)|/\mathcal{G}(\mathbf{r}_c) \in [1,2] \Rightarrow$ intermediate character, $|\mathcal{V}(\mathbf{r}_c)|/\mathcal{G}(\mathbf{r}_c) \in [0,1] \Rightarrow$ long range, weak

2. We pinpoint and characterize the specific molecular orbitals in the NBO picture that are responsible for the intermolecular interactions. We calculate orbital interaction energies up to a second order of perturbation via

$$E_{d \to a}^{(2)} = q_d \frac{|\langle \phi_d |\mathcal{F}| \phi_a \rangle|^2}{E_d - E_a} \tag{1}$$

where $\langle \phi_a |\mathcal{F}| \phi_d \rangle$ are the matrix elements representing the Fock operator in the basis of molecular orbitals which donate (ϕ_d) charge in one fragment and accept (ϕ_a) charge in the other. This quantity measures the deviation of a particular structure from a localized pair–wise Lewis distribution of electrons in molecular orbitals and is directly related to the strength of the interaction.[101,102]

All QTAIM related calculations were carried out using the AIMAll suite.[103] All NBO descriptors were drawn using the NBO 7.0 program[104] as implemented in Gaussian16.[84]

2.3   Calculation of UV–VIS absorption spectra

Since one of the goals of this work is to develop a reliable computational protocol for accurate calculation of absorption spectra of solvated ions, we added progressive levels of sophistication to our approach in the following manner: (i) we calculated absorption spectrum for aqueous nitrite under the PCM model[37–42] with no explicit waters (ii) we took the molecular geometries obtained from the ASCEC search and calculated the corresponding spectra for each bare cluster. In addition to the individual spectra, for every molecularity, we report statistically weighted average spectra (iii) we repeated the previous item adding the solvent under the Integral Equation Formalism (IEF) PCM model with default molecular cavities.

We will address this method as ASCEC + PCM (*iv*) From each of the 200 frames drawn from the MD calculations, we extracted a nano–droplet containing NO_2^- at the center and all water molecules within a 1.4 nm radius. (*v*) We computed the absorption spectra using TD–DFT under QM/MM with just the central NO_2^- ion as the quantum region; the classical solvent was treated using a fluctuating charges (FQ) force field with Rick parameters[105] and another different parametrization.[106] Fluctuating charges and fluctuating dipoles[44] (FQFμ) were used as well. This procedure has been used before in closely related systems and 1.4 nm was proven to accurately match experimental spectra in bulk samples of substantially larger solutes.[28] For all these FQ cases, Pauli repulsion effects,[107,108] "rep", were added. (*vi*) We repeated item (*v*) expanding the quantum region to include the first solvation shells as determined by the first peak of the radial distributions obtained from the MD runs. We will call this solvation model $QM/QM_w/FQ$ in what follows.

In all (*i*−*vi*) cases we used Gaussian16[84] to calculate UV–VIS absorption using TD–DFT accounting for 12 excited states under the B3LYP/6–311++G(d,p) model chemistry. The CAM–B3LYP functional was also considered. These combinations of functional/basis set have proven to be accurate in this line of problems.[109] Whenever needed, weighting factors were obtained from a Boltzmann distribution of the isomers at each molecularity. Gaussian functions and a FWHM of 0.4 eV (3226.17 cm^{-1}) were chosen to plot the convoluted spectra. We also analyzed the orbitals involved in the electronic transitions.

3 Results and discussion

Our MD calculations afforded radial distributions for the O$\longleftrightarrow$H, N$\longleftrightarrow$H distances as shown in the left panel of Figure 1. Two well defined solvation shells are seen in the radial distributions, one centered at ≈ 1.85Å and the other at ≈ 3.17Å in the O$\longleftrightarrow$H curve. Notice

that (i) the N$\longleftrightarrow$H curve provides the exact same information, and (ii) the first solvation shell indicates the lengths of the explicit solute$\cdots$solvent hydrogen bonds resulting from the MD simulations, thus the O$\cdots$H HBs are shorter than N$\cdots$H, hence the relative shifts of the curves. Integrating the first bump and accounting for both runs reveals that the running coordination number for the microsolvation of NO_2^- is 4.95 (4.6 and 5.2 have been reported in other works[110,111]). Similarly, there are 11.45 water molecules up to the second solvation shell. From these results, following the protocol described in the Methods section, we show in the middle panel an individual structure among the 200 randomly chosen frames needed to compute the QM/MM absorption spectra considering the bare NO_2^- as the quantum region. An individual structure showing a quantum region comprising NO_2^- and six water molecules in direct contact with the solute is also shown in the right panel.
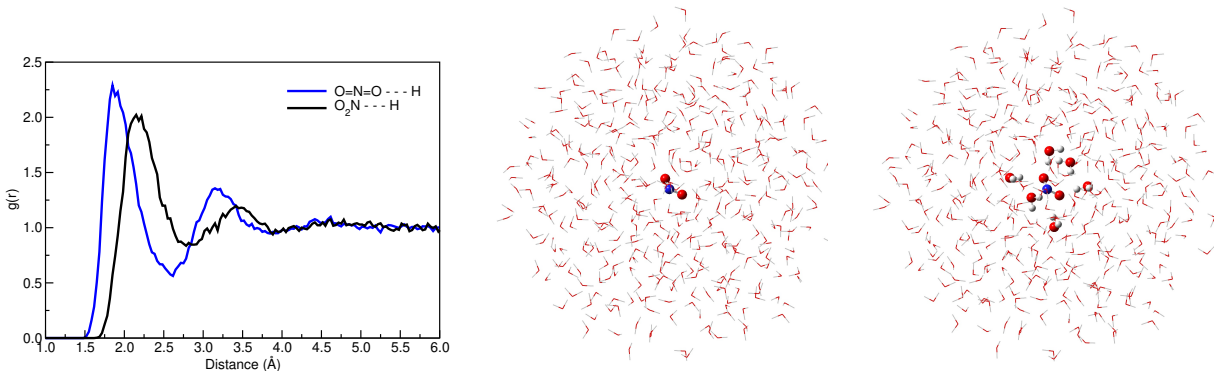

Figure 1: Left: radial distribution functions (RDFs) obtained from one MD run (CM5 charges[71]) simulating NO_2^- in an aqueous environment. RDFs for MD runs using RESP[72] charges are reported in Figure S1 in the ESI. Two individual structures among the 200 randomly chosen frames needed to calculate the QM/MM absorption spectra in each case are shown. The case of the bare NO_2^- quantum region is shown in the middle panel and the case of the quantum region defined by six water molecules in direct contact with NO_2^- is shown in the right panel.

A considerable more detailed picture of the microsolvation of NO_2^- is obtained from the stochastic sampling of the potential energy surfaces of the $[NO_2(H_2O)_x]^-$ clusters with $x = 1-6$. As listed in Table 1, a total of 269 well defined equilibrium structures were located in this work (see the Electronic Supplementary Information for the corresponding geometries, Cartesian coordinates, and properties). From this set, a smaller subset of representative

structures, including in most cases the two lowest minima in each of the Gibbs free energy (298.15 K, 1atm) PES and in the ZPE–corrected electronic PES is shown in Figure 2. The associated energy quantities are listed in Table 2. The entire set of structures is depicted in Figures S2, S3, S4, S5, S6, S7 of the electronic supplementary information. Energies for all structures are available in Table S3 of the SI. It is worth noticing that compact structures are favored in the electronic PES while the inclusion of entropy, temperature and internal degrees of freedom in the Gibbs surfaces favors more open structures, this is consistent with approaching the ideal gas conditions (no intermolecular interactions) when temperature increases.

Table 1: Structural complexity of the B3LYP/6–311++G(d, p) potential energy surfaces for the microsolvation of NO_2^- with up to $x = 6$ explicit water molecules. All minima are within ΔE, ΔE_H, and ΔE_G kcal/mol of the corresponding global minimum using the ZPE–corrected electronic energies, Enthalpies (298.15 K, 1 atm), and Gibbs energies (298.15 K, 1 atm), respectively.

x	Number of isomers	ΔE	ΔE_H	ΔE_G
1	4	2.64	2.65	2.55
2	9	2.88	2.70	3.16
3	30	4.67	4.81	4.94
4	48	6.18	6.68	7.17
5	68	10.36	11.07	10.74
6	110	17.23	17.26	20.75

The first observation from Tables 1 and 2 and from the extended data in Table S3 in the electronic supplementary information is that the $[NO_2 (H_2O)_x]^-$ surfaces are heavily populated within small energy windows, thus, because of the isomer populations, several structures should have significant contributions to experimental observations. Case in point is the experimentally measured sequential enthalpies of hydration, defined as the enthalpies involved in the $[NO_2 (H_2O)_{x-1}]^- + H_2O \rightarrow [NO_2 (H_2O)_x]^-$ reaction for each x. As shown in Figure 3, the computed values accurately match the experimental data[112] when the sequential enthalpies are calculated assigning a weighted contribution from each isomer given by the isomer population derived from a standard Boltzmann distribution.
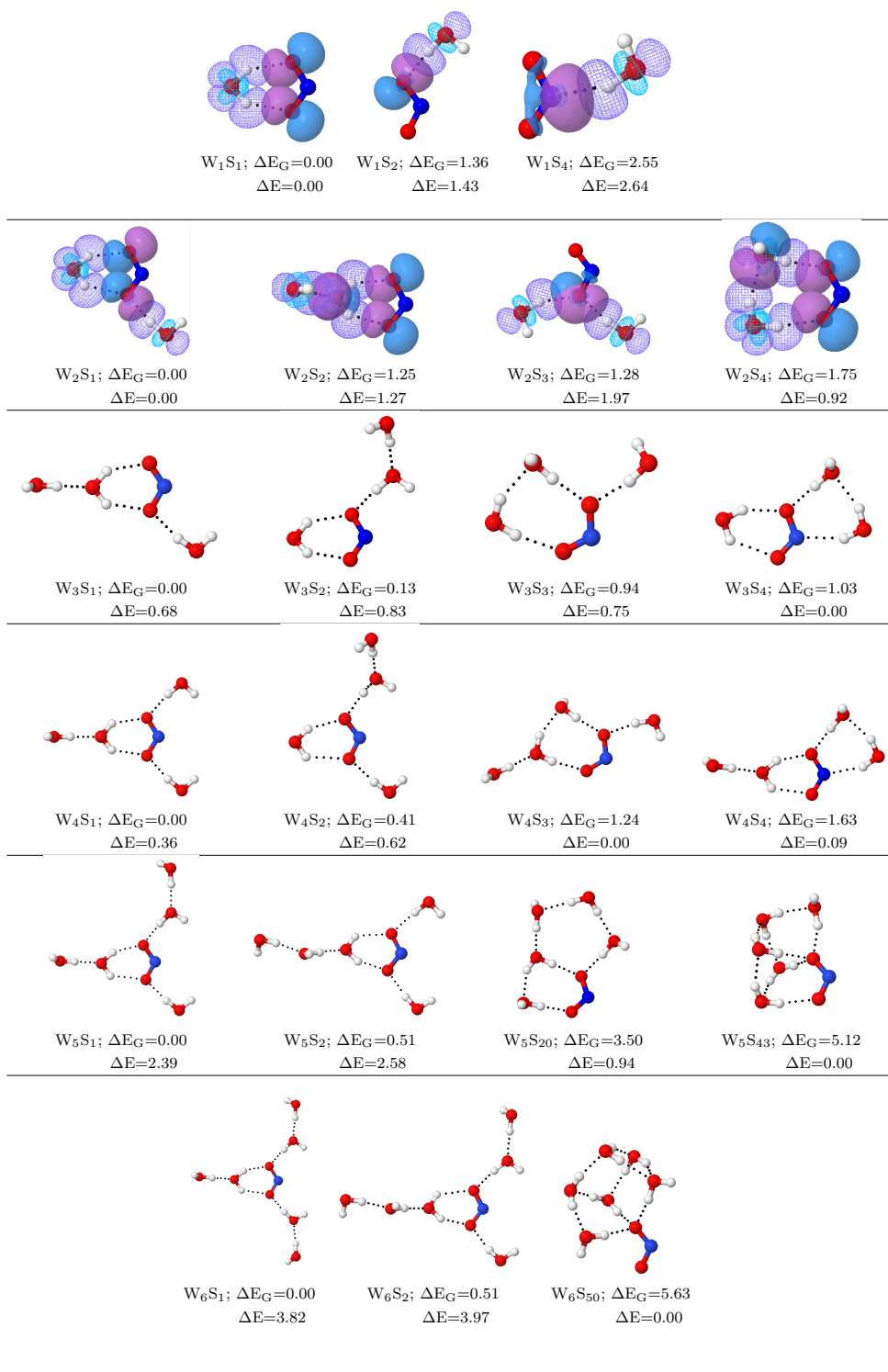
W$_1$S$_1$; ΔE$_G$=0.00   W$_1$S$_2$; ΔE$_G$=1.36   W$_1$S$_4$; ΔE$_G$=2.55
ΔE=0.00 ΔE=1.43 ΔE=2.64

W$_2$S$_1$; ΔE$_G$=0.00   W$_2$S$_2$; ΔE$_G$=1.25   W$_2$S$_3$; ΔE$_G$=1.28   W$_2$S$_4$; ΔE$_G$=1.75
ΔE=0.00 ΔE=1.27 ΔE=1.97 ΔE=0.92

W$_3$S$_1$; ΔE$_G$=0.00   W$_3$S$_2$; ΔE$_G$=0.13   W$_3$S$_3$; ΔE$_G$=0.94   W$_3$S$_4$; ΔE$_G$=1.03
ΔE=0.68 ΔE=0.83 ΔE=0.75 ΔE=0.00

W$_4$S$_1$; ΔE$_G$=0.00   W$_4$S$_2$; ΔE$_G$=0.41   W$_4$S$_3$; ΔE$_G$=1.24   W$_4$S$_4$; ΔE$_G$=1.63
ΔE=0.36 ΔE=0.62 ΔE=0.00 ΔE=0.09

W$_5$S$_1$; ΔE$_G$=0.00   W$_5$S$_2$; ΔE$_G$=0.51   W$_5$S$_{20}$; ΔE$_G$=3.50   W$_5$S$_{43}$; ΔE$_G$=5.12
ΔE=2.39 ΔE=2.58 ΔE=0.94 ΔE=0.00

W$_6$S$_1$; ΔE$_G$=0.00   W$_6$S$_2$; ΔE$_G$=0.51   W$_6$S$_{50}$; ΔE$_G$=5.63
ΔE=3.82 ΔE=3.97 ΔE=0.00

Figure 2: A small sample of the structural variety found in this work for the microsolvation of NO$_2^-$ with up to six explicit water molecules at the B3LYP/6–311++G(d,p) level. Only a few of the lowest energy structures in the Gibbs (ΔE$_G$ kcal/mol with respect to the global minimum) and in the ZPE–corrected electronic (ΔE kcal/mol with respect to the global minimum) potential energy surfaces are shown, see Figures S2, S3, S4, S5, S6, S7 in the electronic supplementary information for the entire set. All QTAIM derived intermolecular interactions are shown as dotted lines and a few illustrative examples of the $n_O \rightarrow \sigma^*_{O-H}$ and $n_N \rightarrow \sigma^*_{O-H}$ orbital interactions stabilizing the clusters are shown.

Table 2: Binding energies in kcal/mol and isomer populations ($\%\chi_i$) derived from Boltzmann distributions of the isomer energies for the set of structures shown in Figure 2. B3LYP ZPE corrections to the electronic energy are used when needed. We list electronic (E), Counterpoise corrected for BSSE (E_{CP}), DLNPO–CCSD(T) (E_{CC}), Enthalpy (H) and Gibbs (G, room conditions) energies.

| Structures	$-$BE	$-$BE$_{CP}$	$-$BE$_{CC}$	$-$BE$_H$	$-$BE$_G$	$\%\chi_i$E	$\%\chi_i$H	$\%\chi_i$G
W_1S_1	16.13	15.13	15.60	16.72	8.01	89.51	90.52	85.30
W_1S_2	14.69	14.05	14.41	15.24	6.65	7.95	7.40	8.60
W_1S_3	13.49	12.84	12.48	14.08	5.46	1.04	1.04	1.15
W_2S_1	28.57	26.90	28.26	29.49	12.64	66.87	53.00	74.90
W_2S_2	27.30	25.23	26.28	28.44	11.39	7.88	8.93	9.15
W_2S_3	26.60	25.10	26.23	27.34	11.36	2.39	1.41	8.59
W_2S_4	27.65	25.91	26.89	29.00	10.89	14.19	23.32	3.92
W_3S_1	38.59	35.96	37.88	39.94	15.16	7.58	4.04	27.90
W_3S_2	38.44	35.78	38.03	39.82	15.04	5.91	3.32	22.57
W_3S_3	38.53	36.15	38.18	40.09	14.22	6.77	5.26	5.67
W_3S_4	39.28	36.72	38.98	41.00	14.13	24.04	24.29	4.90
W_4S_1	48.50	45.30	48.02	49.96	17.75	5.49	1.42	46.46
W_4S_2	48.24	45.01	47.89	49.75	17.34	3.54	0.99	23.44
W_4S_3	48.85	45.38	48.32	50.91	16.51	10.02	7.05	5.76
W_4S_4	48.77	45.18	48.39	50.88	16.12	8.66	6.74	2.97
W_5S_1	57.05	52.95	56.49	58.83	18.92	0.69	0.04	34.97
W_5S_2	57.20	53.01	56.68	59.08	18.90	0.88	0.05	33.73
W_5S_{20}	58.51	53.67	57.94	61.74	15.42	8.04	4.86	0.10
W_5S_{43}	59.44	54.22	60.81	63.35	13.80	39.15	72.56	0.01
W_6S_1	65.30	60.33	64.62	67.33	20.28	0.12	0.00	56.99
W_6S_2	65.15	60.18	64.33	67.33	19.38	0.10	0.00	12.49
W_6S_{50}	69.12	62.63	70.63	73.70	14.65	78.73	90.76	0.00
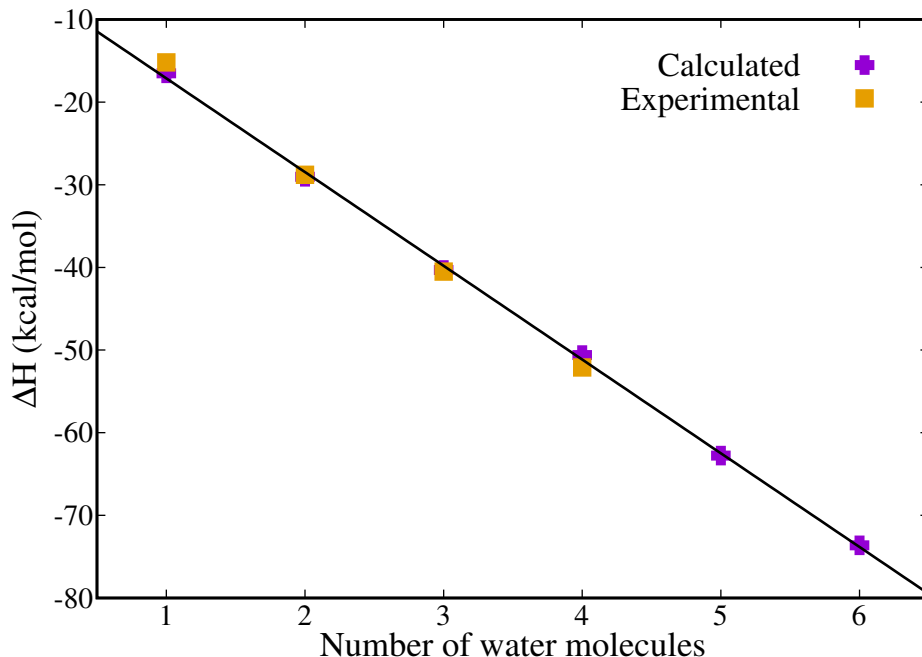
Figure 3: Sequential hydration enthalpies for NO_2^-. Experimental Enthalpies of Hydration are taken from Lee et al.[112]

Notice that binding energies for $[NO_2\,(H_2O)_x]^-$ are quite similar to those obtained during the microsolvation of NO_3^-, another monovalent multiatomic anion, which run in the -15.25 to -73.53 kcal/mol range in going from $x = 1$ to $x = 6$ for the ZPE–corrected electronic energies,[113] and are substantially smaller than the binding energies obtained for divalent SO_4^-, which run in the -27.70 to -133.84 kcal/mol interval.[114] Table 2 also shows that binding energies are not too sensitive to the basis set superposition error (BSSE, maximum deviation $\approx 7\%$), as has been documented for other types of charged[113] and neutral clusters.[115,116] The effect of dispersion is even smaller (compare the B3LYP and DLPNO–CCSD(T) columns in Table 2). Notice that the experimental sequential hydration enthalpies in Figure 3 are accurately reproduced without the need for BSSE corrections or dispersion.

It has been shown that formally charged species have a marked chaotropic effect in the surrounding water to water hydrogen bonding network of the solvent molecules.[67,98,113,114,117–126] Fittingly, in our particular case, Figure 4 shows that under the influence of the formal charge

in NO_2^-, not all hydrogen bonds are the same: there are at least two types of $H_2O \cdots H-O-H$ interactions (two blue peaks in the right panel) centered at ≈ 1.82 and 2.01 Å, a stark contrast to pure water tetramers,[82] pentamers,[127] hexamers[128] and heptamers,[129] where hydrogen bonds are homogeneously center around ≈ 1.97 Å, precisely the distance obtained for the hydrogen bond in the water dimer at the same level of this study. Under the premise that for the specific hydrogen bonds stabilizing the title clusters, an intuitive inverse relationship between bond length and strength holds (see below for a formal analysis of the strength of the interactions), Figure 4 hints at a hierarchy of interaction strength established by the following scale: $O=N=O \cdots H-O-H$ (1.79 Å) > $H_2O \cdots H-O-H$ (1.82 Å) > $O_2N \cdots H-O-H$ (1.89 Å) > $H_2O \cdots H-O-H$ (2.01 Å).
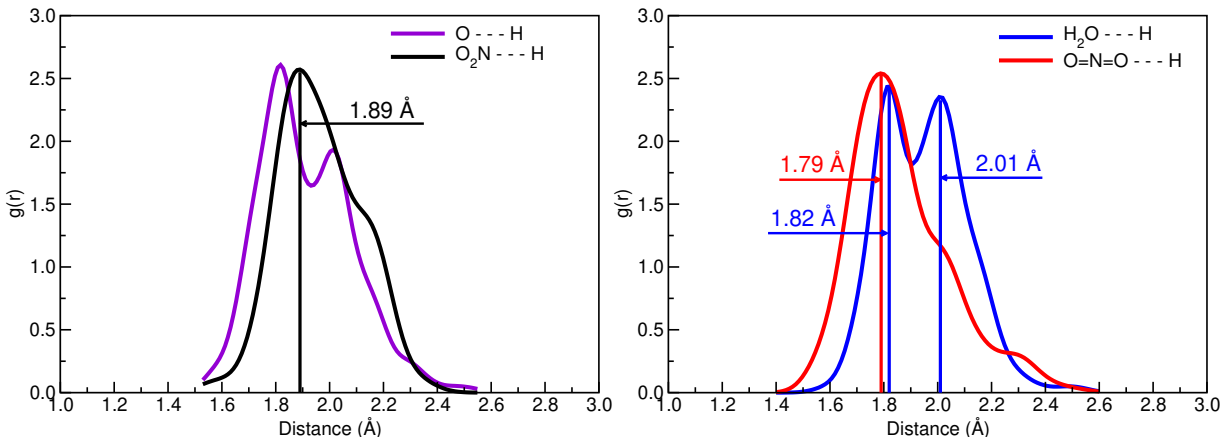
Figure 4: Radial distribution functions for hydrogen bond distances in the microsolvation of NO_2^- with up to six explicit water molecules at the B3LYP/6–311++G(d, p) level. The purple line in the left panel shows all $O \cdots H$ hydrogen bonds, which are split into $O=N=O \cdots H$ and $H_2O \cdots H-O-H$ in the right panel.

3.1 Bonding

As in previous studies,[130] our results show that only three distinct types of hydrogen bonds are at play stabilizing the clusters: $O=N=O \cdots H-O-H$, $H_2O \cdots H-O-H$, and $O_2N \cdots H-O-H$, whose relative strengths have been broadly categorized based on the length of the corresponding set of HBs. We offer next a more detailed dissection of the intermolecular bonding interactions. For all bond critical points representing intermolecular hydrogen bonds

in this work $\nabla^2\rho\left(\mathbf{r}_c\right) > 0$, thus, item $1(a)$ in section 2.2 indicates that in a general sense all intermolecular contacts are to be characterized as weak, long range. Figure 5 plots the distributions of all other AIM descriptors along the found ranges of values. The chaotropic effect of the formal charge on the solvent hydrogen bonds is clearly seen in the splitting of the $H_2O\cdots H\text{--}O\text{--}H$ curves in all cases: two well defined peaks in the densities plot and distinctive shoulders in the virial ratios and in the energy densities. Furthermore, taking the properties of the hydrogen bond for the isolated water dimer (W_2) as reference, a sensible charge induced strengthening of the HBs in the solvent is systematically seen from all plots as (i) a second peak with larger accumulations of electron densities (ii) an increase in the virial ratio with respect to W_2, and (iii) smaller bond degree parameters. Interestingly, the three factor combination of large electron densities, negative total energy densities, and virial ratios larger than 1 suggests that a sizable number of solute$\longleftrightarrow$solvent and solvent$\longleftrightarrow$solvent contacts should actually be characterized as strong hydrogen bonds without reaching covalent status despite the negative bond degree parameters.[97]

The QTAIM plots offer some additional subtle interesting details: notice that according to the trends to the right of the virial ratios and BCP densities plots and to the left of the bond degree parameter plot, the strength of the interactions follows the established $O\text{=}N\text{=}O\cdots H\text{--}O\text{--}H > H_2O\cdots H\text{--}O\text{--}H > O_2N\cdots H\text{--}O\text{--}H > H_2O\cdots H\text{--}O\text{--}H$ hierarchy, which for the most part determines relative cluster stability, however, the intermediate sections of the plots show that, away from the strongest interactions, the strengths of the three types of contacts are actually quite competitive. This result is fully consistent with previous studies for the microsolvation of NO_3^- by Acelas and coworkers[113] and by Pathak et. al.[131] where this competition between different charge assisted interactions was rationalized in terms of the available charges and static and dynamic polarizabilities.

The NBO picture of bonding interactions is fully consistent with the information drawn from the AIM descriptors. That is,
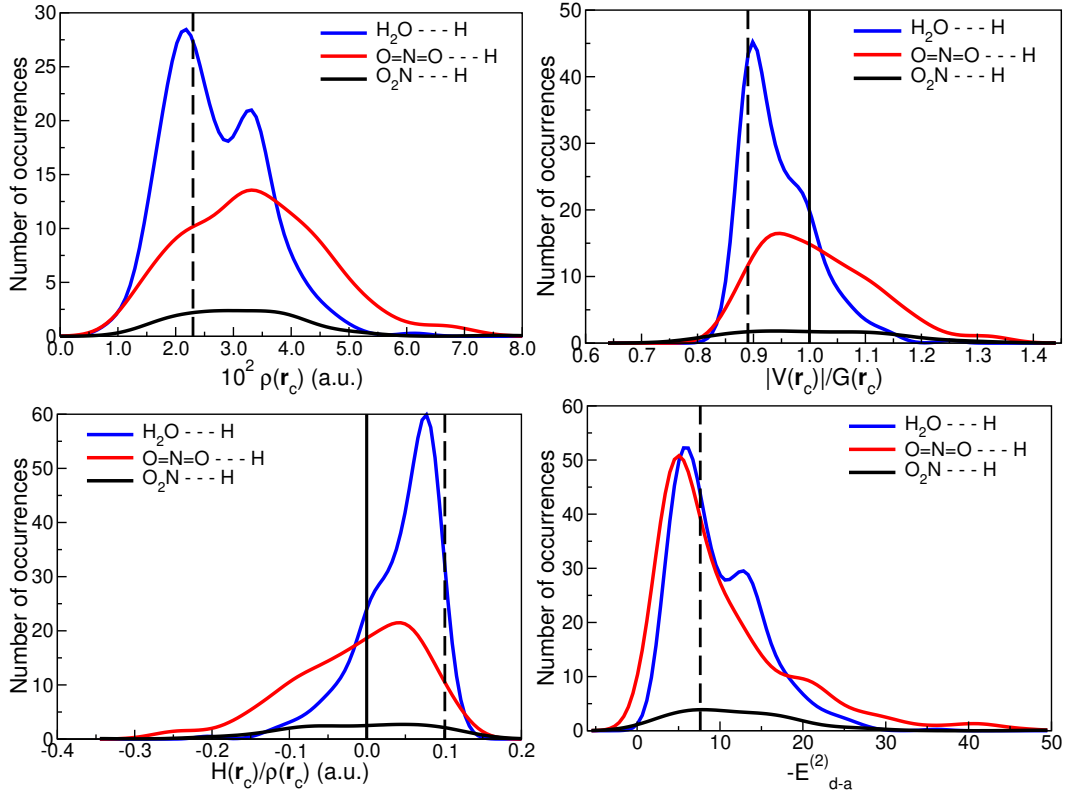
Figure 5: Distributions of QTAIM descriptors of the strength of intermolecular hydrogen bonds in the microsolvation of NO_2^- with up to six explicit water molecules (all 269 equilibrium structures are included). Dashed vertical lines indicate the values obtained for the reference hydrogen bond in the isolated water dimer. Vertical solid lines represent the rigid $|\mathcal{V}|/\mathcal{G} = 1.0$ and $\mathcal{H}/\rho = 0$ boundaries established in section 2.2. The bottom right panel shows the distributions of orbital interaction energies given by $-E_{d \to a}^{(2)} > 3.0$ kcal/mol (Eqtn. 1) for the corresponding bond critical points.

1. The three intermolecular contacts are well characterized by the following charge assisted hydrogen bonds arising from donor $\rightarrow$ acceptor orbital interactions:

   (a) O=N=O$\cdots$H–O–H are due to $n_O \rightarrow \sigma^*_{O-H}$ (structure W_1S_1 in Figure 2)

   (b) O$_2$N$\cdots$H–O–H are due to $n_N \rightarrow \sigma^*_{O-H}$ (structure W_1S_3 in Figure 2)

   (c) H$_2$O$\cdots$H–O–H are due to $n_O \rightarrow \sigma^*_{O-H}$ (structure W_2S_4 in Figure 2)

2. The chaotropic effect of the formal charge in the hydrogen bond network among water solvents is seen in the splitting into two peaks of the orbital interaction energies with most of the energies close to the reference isolated water dimer but with a sensible number of strengthened contacts collected in the smaller peak to the right with higher energies

3. As in QTAIM, all intermolecular contacts are characterized by NBO as long range as well because without exception, fragment to fragment interaction is described by $\phi_d \rightarrow \phi_a$ orbital interactions with no formation of bonding σ orbitals between the two molecules

4. The competition between the three specific types of contacts in the regions away from the strongest interactions is also clearly seen

We point out that as in the microsolvation of other charged species,[114,118,122] Figures S2-S7 and the set of Cartesian coordinates provided in the electronic supplementary material indicate that the chaotropic effect of the formal charge leads to situation where partial dissociation of water molecules is attained. This is quite interesting from the perspective of chemical bonding because it transcends the classical classifications of chemical bonds and long range interactions and shows that equilibrium structures with partial bonds may be found in nature. Notwithstanding their high relative energy and thus their small statistical weight and small contributions to macroscopic properties, those structures are included in

the calculation of ASCEC derived spectra, which, as discussed below, afford outstanding matchings to experimental measurements.

3.2 Spectra

The electronic structure of isolated NO_2^- was experimentally established in 1957 by Sidman.[61] In Figure 6, we report a pictorial representation of the significant molecular orbitals of isolate NO_2^- as calculated at the B3LYP/6-311++G(d,p) level, and we assign them by following the nomenclature provided in Ref. 61.

Aqueous nitrite has been characterized using UV–Vis absorption spectra.[51,55–62] Experimental conditions (temperature, pressure) seem to have little effect on the quality of the signals, however, concentration and the presence of external agents in the analyte (counterions, etc.) pose a greater challenge, considerably affecting both the position and intensities of the bands. A summary of the most relevant features of the spectra is presented in Table 3.

Table 3: Summary of experimental features and conditions for the UV–Vis absorption spectra of aqueous NO_2^-

Source	λ_{max} (nm)	Concentration
Aluker et al.[51]	210	$0.1 - 200$ mg/L
	355	$20 -$ mg/L
Ianoul et al.[55]	210	7×10^{-5} M
Opländer and Suschek[56]	$340 - 360$ band	2.5×10^{-2} M
Thomas and Brogat[57]	212.8	10.6 mg/L
	353.9	3007 mg/L
Zuo and Deng[58]	354 weak band	$5 \times 10^{-3} - 4 \times 10^{-2}$ M
	292 weak shoulder	
Mizuno et al.[59]	210	1.8×10^{-4} M
Friedman[60]	211	$7 \times 10^{-5} - 6 \times 10^{-3}$ M

In order to assess the reliability of the various computational approaches used in the present work, we take as reference the experimental spectra reported by Thomas and Brogat,[57] and in particular the intense band at 212.8 nm, and the weak band at 353.9 nm.

Molecular Orbital	Isolated NO_2^-	ASCEC Cluster	ASCEC Cluster + PCM	$QM/QM_w/FQ$
π^*				
n_N				
n_{O_2}				
π_2				
π_1				

Figure 6: Molecular orbitals involved in UV–Vis transitions, for the isolated NO_2^-, for the global minimum of the PES for $NO_2^-(H_2O)_6$ and for a randomly selected snapshot extracted from the MD and used in the case of the $QM/QM_w/FQ$ approach. In the $QM/QM_w/FQ$ snapshot, the MM water molecules are not shown. Isovalue= 0.02.

A preliminary analysis performed on the results obtained by modelling the aqueous environment by means of PCM indicates that the intense 212.8 nm band is attributed to $\pi_2 \to \pi^*$ transition from the bare ion (see Figure 6 for notation) with small contributions from $n_{O_2} \to \pi^*$ and $n_{O_1} \to \pi^*$. Similarly, the weak 353.8 nm band is attributed to $n_N \to \pi^*$ transition. By exploiting the microsolvated NO_2^- cluster (Figure 6) approach, we notice that these bands involve non–negligible contributions from transitions between MOs spanned also in the water molecules: $n_N \to \pi^*$ for the weak 353.9 nm band and $n_{O_2} \to \pi^*$, $\pi_2 \to \pi^*$, for the intense 212.8 nm band. Not only do these transitions from cluster orbitals help rationalizing the spectrum, we argue that including them is the only way of ensuring an actual match to the experimental data, therefore, a rigorous exploration of the PESs corresponding to microsolvation is the way to go.

Table 4 lists the computed and experimental data for the absorption spectra of nitrite in aqueous media. Figure 7 displays the corresponding spectra for the different solvation models analyzed in this work. The top left panel of Figure 7 shows that the spectrum of isolated NO_2^- under the continuum solvent (QM/PCM, dashed red line) cannot properly model the experimental data. Since the inclusion of explicit water molecules is mandatory to accurately model solvation in this system, we present next the results for the full QM clusters and for the atomistic QM/MM approaches. Overall, B3LYP does an outstanding good job reproducing the experimental spectra, hence, in what follows, we will only discuss the B3LYP data and place all remaining CAM–B3LYP results in the electronic supplementary material, see Table S5 and Figure S8.

Table 4: Calculated spectral features for solvated NO_2^- using the 6–311++G(d, p) basis set under various methodologies (see section 2 for methods and notation). Experimental $\lambda_{max} = 353.9$ (weak), $\lambda_{max} = 212.8$ nm (intense) as reported by Thomas and Brogat[57] for 10.6 and 3007 mg/L, respectively. x, the number water molecules in direct contact with NO_2^- and W_t, the total number of water molecules surrounding the solute, are included

Sampling	Solvation model	x	W_t	B3LYP		mg NO_2^-/L sln
				$n \to \pi^*$ $\lambda_{max,1}$	$\pi \to \pi^*$ $\lambda_{max,2}$	
Isolated NO_2^-	PCM			371.10	196.44	
ASCEC	Gas phase cluster	1	1	346.59	191.49	
		2	2	365.59	194.83	
		3	3	360.69	230.23	
		4	4	357.01	215.49	
		5	5	355.17	198.82	
		6	6	356.40	198.82	
ASCEC	Cluster + PCM	1	1	373.55	230.61	2.54
		2	2	368.04	217.06	1.27
		3	3	365.59	218.13	0.85
		4	4	359.46	212.41	0.64
		5	5	357.01	215.63	0.51
		6	6	357.01	211.34	0.42
MD	QM/FQa		414	337.27	180.51	6.15×10^{-3}
MD	QM/FQa+rep		414	346.98	168.35	
MD	QM/FQb		414	338.07	177.12	
MD	QM/FQb+rep		414	347.95	167.67	
MD	QM/FQFμ		414	337.72	178.70	
MD	QM/FQFμ + rep		414	347.71	169.03	
MD	QM/QM$_w$/FQa	7	414	352.86	189.32	
MD	QM/QM$_w$/FQa	11	414	352.86	199.76	
MD	QM/QM$_w$/FQa	16	414	353.11	208.51	

3.2.1 ASCEC derived spectra

Table 4 and Figure 7 compare the experimental[57] against the calculated spectra for the configurations drawn from the structural sampling using the ASCEC algorithm for $[NO_2 (H_2O)_x]^-$, $x = 1 - 6$ (see section **??** above). Standard Boltzmann distributions of the isomers were used to assign weighting factors in the statistically averaged spectra for each molecularity, namely, rather than just calculating the spectra using only the global minimum in each case,
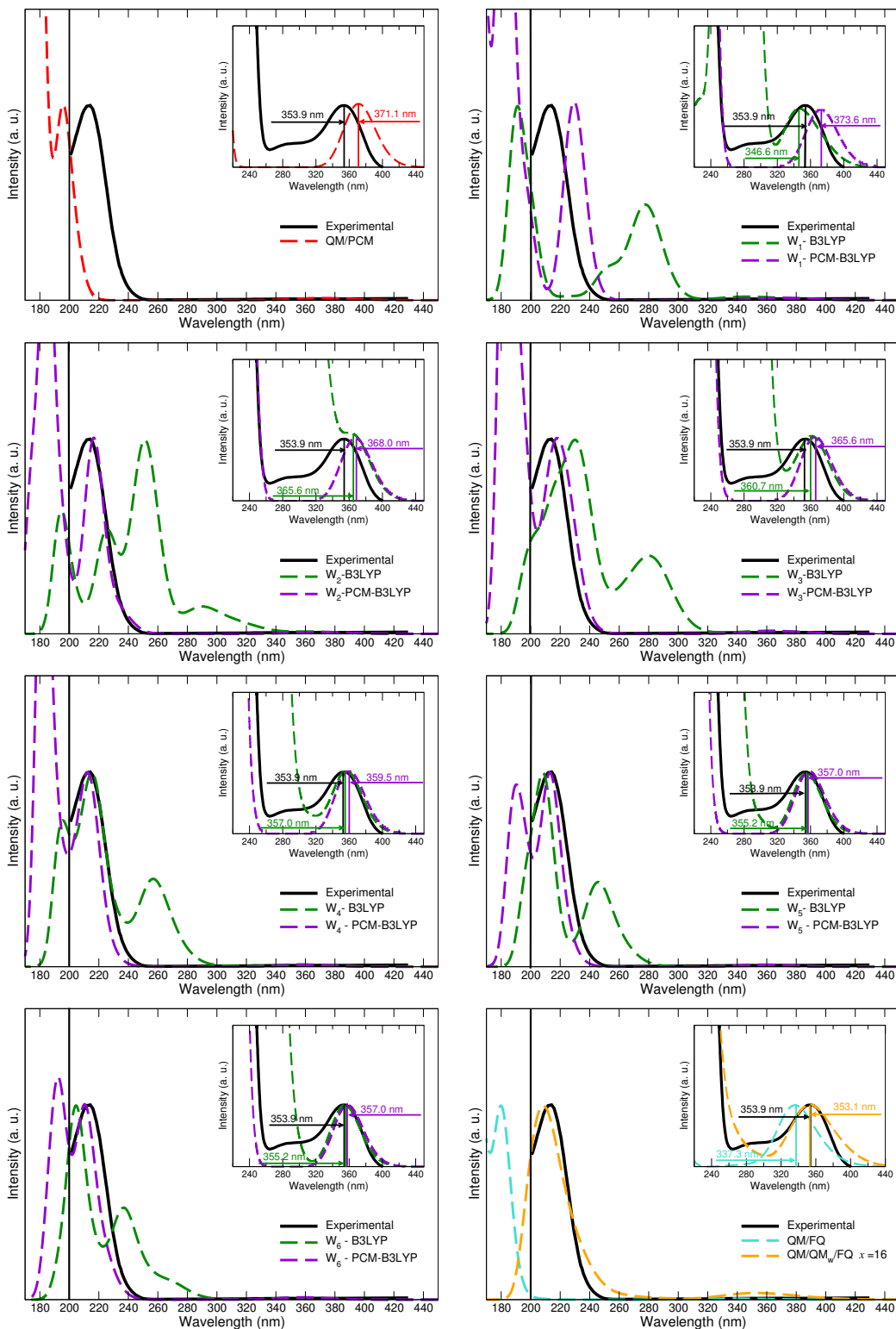
Figure 7: Experimental[57] (solid black line) and computed (dashed lines) spectra for aqueous nitrite. See section 2 for details of the calculations. There is no experimental information to the left of the vertical solid lines. An inset showing the structure of the low intensity 353.9 nm band is also provided. See Table 4 for the experimental and simulated concentrations.

contributions from all isomers are properly accounted.

From the comparison between experiment and computations, it is clear that both ASCEC derived spectra (bare cluster and cluster + PCM) recover the qualitative features of the experimental spectra. Nevertheless, there is an unsatisfactory quantitative agreement between the calculated spectra for bare gas phase clusters (dashed green lines) and the experimental (solid black lines) results for all molecularities for the 212.8 nm band. Conversely, for the same 212.8 nm band, as the number of explicit water molecules increases, the quantitative agreement between the cluster + PCM spectra (purple dashed lines) systematically improves to the point that impressive matches are obtained for $x \geq 5$. The weak 353.9 nm band seems not as sensitive to including the solvent via PCM with both spectra showing good quantitative agreement in λ_{max} which again improves as x grows. From the above observations, $x = 6$ seems more than adequate to reproduce the qualitative and quantitative features of the experimental spectra.

3.2.2 MD derived spectra

In parallel with the full QM spectra, an atomistic QM/MM approach, coupled to molecular dynamics (MD) simulations, was also examined for simulating the electronic absorption spectrum of solvated nitrite. Plots of the MD derived spectra are depicted in Figure 7 and the wavelengths for the maxima of the absorption bands are listed in Table 4. The MM portion was treated by using the Fluctuating Charge (FQ)[4,43] or Fluctuating Charge and Fluctuating Dipoles (FQFμ) force fields.[44,45] Two different parametrizations were exploited in case of QM/FQ calculations, named FQa from[105] and FQb from.[106] In both approaches, the mutual QM–MM polarization effects are taken into account. Pauli repulsion contributions (named +rep) were also considered by using the model developed by some of the present authors.[107,132]

Several tests were conducted in order to choose the best computational protocol in QM/MM simulations. To this end, different solute charges (RESP[72] vs CM5[71]) and different sphere radii were used. We first note that the position of the $n \to \pi^*$ band slightly redshifts up to 3 nm going from CM5 to RESP charges (see Table S4 in ESI). Such a difference may be attributed to shorter N$\cdots$H distances obtained from MD runs using RESP charges (Figure S1 in the ESI), thus directly affecting the nitrogen lone pair involved in the considered transition. Similarly, the size of the sphere does not have an impact on the vertical excitation energies, yielding similar results when moving from 14 Å to 18 Å , i.e. when a higher number of MM water molecules is accommodated within the sphere (414 vs. 864). Therefore, the QM/MM results can be considered at convergence with respect to the size of the droplet.

In all evaluated cases, the polarizable QM/FQ scheme provided excitation energies that differ from the experimental values, even though the inclusion of the Pauli repulsion term in the QM/MM interaction energy moves the position of the $n \to \pi^*$ band in the right direction, while wrongly shifting the $\pi \to \pi^*$ band to shorter wavelengths. The same comment is valid also when the electrostatic interactions are refined through the inclusion of polarizable dipoles in the MM portion (see QM/FQFμ results). It is worth mentioning that when the solvation phenomenon is modelled *via* QM/FQ(Fμ), both electrostatic and polarization contributions are taken into account. When Pauli repulsion effects are also included, the interactions described by the QM/classical approach do not, in principle, differ from those treated at the full QM level in the ASCEC sampling, since dispersion effects are not taken into account by both methods. However, the polarizable QM/FQ(Fμ) + rep results differ from the ASCEC computed data, which for this particular problem provide a better reproduction of the experimental spectrum.

To justify the differences between the QM/MM and ASCEC results, we follow recent works[108] and include in the QM region of the QM/MM modeling, all the water molecules

that are closest to NO_2^-. As listed in Table 4, radial distribution functions (Figure S1 in the ESI) afford 7, 11, 16 solvent molecules for the first, second, and third solvation shells respectively. Therefore, such water molecules were used to define the quantum region in the $QM/QM_w/FQa$ calculations. Under this approach, the computed vertical excitation energies shift systematically closer to the experimental values. In fact, the $\pi \rightarrow \pi^*$ band redshifts from 189.32 ($x = 7$ W) to 199.76 ($x = 11$ W) to 208.51 nm ($x =16$ W). The systematic improvement of the results may be explained by analyzing the molecular orbitals involved in the main transitions. In Figure 6, five selected molecular orbitals of the global minimum for $NO_2^-(H_2O)_6$ found with the ASCEC method are depicted along with the same orbitals for a randomly selected snapshot extracted from the MD and used in the case of the $QM/QM_w/FQ$ approach. By taking a look at the MOs in the full QM cases, it is clear that charge transfer between solute and solvent is an active component of molecular orbitals contributing to the 212.8 nm band, thus implying that the orbitals involved belong not just to the nitrite but also to the nearest water molecules. In view of the above findings, it is clear why the inclusion of Pauli repulsion effects deteriorated the agreement with the experimental findings for the 212.8 nm band. Finally, we conclude that the inclusion of solute↔solvent charge transfer (CT), which are not yet introduced in any QM/classical model, is mandatory for the correct description and reproduction of the experimental spectra of nitrite ion in aqueous solution.

Notice that other works have focused on the calculation of X–ray absorption spectra of solvated aqueous NO_2^- , using QM/MM with the quantum region calculated at the semi–empirical PM3 level and the classical region under the Amber force field with 90 and 550 water molecules.[133] Similarly to our results, their calculated spectra reproduced the experimental measurements for nitrate and nitrite after transferring the closest water molecules from the classical to the quantum region. Fittingly, they also found that the orbitals in the water molecules are involved in the electronic transitions determining the absorption spectra, again in agreement with our findings. Remarkably, the QM/MM approach used in the

27

present work substantially differs from that exploited in Ref. 133 because in the latter the QM region is described at a lower level of theory through a semi-empirical method, while the MM portion is treated by means of a standard non-polarizable force field. The polarization of the MM portion can be particularly crucial for the calculation of spectroscopic properties because it results in specific terms entering the response equations of the system. In addition, in our approach, the interaction between the QM and MM regions is not limited to electrostatics, but also includes Pauli repulsion effects explicitly dependent on the QM density. Such interactions seem not to be particularly relevant for the reproduction of the experimental spectrum, however they help identify and dissect the origin of the experimental signal in terms of the solute-solvent interactions: since the $QM/FQ(F\mu)$+rep model includes all but charge-transfer effects which are instead present when some water molecules are included in the QM system, they evidently play a critical role. Finally, we notice that the theoretical modelling of core-excitations presents some difficulties and peculiarities which are not present in calculations of valence transitions, therefore conclusions about valence excitations may not necessarily be immediately transferable to core excitations.

4 Summary and conclusions

A study of the absorption spectra of aqueous NO_2^- under different approaches is presented in this work. Our analysis shows that in order to accurately reproduce experimental results it is necessary to rigorously sample the quantum potential energy surfaces for microsolvation of NO_2^- with at least five explicit water molecules and then calculate the absorption spectrum of the clusters embedded in a continuum solvent accounting for the statistical weighted contributions of individual isomers. We address this procedure as ASCEC + PCM. An alternative computational strategy, affording equally outstanding matches against the experimental results involves running MD simulations with classical potentials on systems with large numbers of water molecules and then calculating QM/MM spectra where the QM

region is defined by all water molecules contained up to the third solvation shell, while the MM region can be safely modeled by classical waters. However, despite the excellent spectra, compared against the samplings of the microsolvation PESs, the snapshots extracted from MD simulations require a larger number of explicit water molecules in the QM region (up to 16), do not provide the well defined minima in the quantum PES needed for the calculation of vibrational frequencies.

We expect the ASCEC + PCM combination to be of general applicability to model absorption spectra of negatively charged species with the proper variation on the number of explicit quantum waters depending on the particular problem. Because of the outstanding reproduction of the absorption spectra of aqueous nitrite, and of the experimental sequential hydration enthalpies, which in fact validates the configurational sampling, we expect this methodology to provide the configurations needed to obtain vibrational spectra, as well as mixed electronic-vibrational properties such as resonance Raman spectra, whose calculations are underway in an effort to develop a computational methodology to guide the experimental detection and quantification of NO_2^- in aqueous samples that may include other contaminants, effectively eliminating all intermediate separation and isolation steps from present day analytical protocols.

Acknowledgement

Supporting Information Available

Description of the MD and ASCEC simulations. Radial distribution functions from the MD simulations. Energies and isomer populations afforded by ASCEC. Structural motifs. Vertical excitation energies. CAM–B3LYP spectra. Cartesian coordinates for the equilibrium structures afforded by ASCEC.

References

(1) Mennucci, B. Modeling environment effects on spectroscopies through QM/classical models. *Phys. Chem. Chem. Phys.* **2013**, *15*, 6583–6594.

(2) Olsen, J. M. H.; Steinmann, C.; Ruud, K.; Kongsted, J. Polarizable density embedding: A new QM/QM/MM-based computational strategy. *J. Phys. Chem. A* **2015**, *119*, 5344–5355.

(3) Mennucci, B. Polarizable continuum model. *Wiley Interdisciplinary Reviews: Computational Molecular Science* **2012**, *2*, 386–404.

(4) Giovannini, T.; Egidi, F.; Cappelli, C. Molecular spectroscopy of aqueous solutions: a theoretical perspective. *Chem. Soc. Rev.* **2020**, *49*, 5664–5677.

(5) Egidi, F.; Segado, M.; Koch, H.; Cappelli, C.; Barone, V. A benchmark study of electronic excitation energies, transition moments, and excited-state energy gradients on the nicotine molecule. *The Journal of chemical physics* **2014**, *141*, 224114.

(6) Kitaura, K.; Ikeo, E.; Asada, T.; Nakano, T.; Uebayasi, M. Fragment molecular orbital method: an approximate computational method for large molecules. *Chemical Physics Letters* **1999**, *313*, 701–706.

(7) York, D. M.; Lee, T.-S.; Yang, W. Quantum Mechanical Study of Aqueous Polarization

Effects on Biological Macromolecules. *Journal of the American Chemical Society* **1996**, *118*, 10940–10941.

(8) Giese, T. J.; Huang, M.; Chen, H.; York, D. M. Recent Advances toward a General Purpose Linear-Scaling Quantum Force Field. *Accounts of Chemical Research* **2014**, *47*, 2812–2820, PMID: 24937206.

(9) Xie, W.; Gao, J. Design of a Next Generation Force Field: The X-POL Potential. *Journal of Chemical Theory and Computation* **2007**, *3*, 1890–1900, PMID: 18985172.

(10) Giovannini, T.; Egidi, F.; Cappelli, C. Theory and algorithms for chiroptical properties and spectroscopies of aqueous systems. *Phys. Chem. Chem. Phys.* **2020**, *22*, 22864–22879.

(11) Tomasi, J.; Cammi, R.; Mennucci, B.; Cappelli, C.; Corni, S. Molecular properties in solution described with a continuum solvation model. *Phys. Chem. Chem. Phys.* **2002**, *4*, 5697–5712.

(12) Olsen, J. M. H.; Kongsted, J. Molecular properties through polarizable embedding. *Adv. Quantum Chem.* **2011**, *61*, 107–143.

(13) Steindal, A. H.; Ruud, K.; Frediani, L.; Aidas, K.; Kongsted, J. Excitation energies in solution: the fully polarizable QM/MM/PCM method. *J. Phys. Chem. B* **2011**, *115*, 3027–3037.

(14) Curutchet, C.; Muñoz-Losa, A.; Monti, S.; Kongsted, J.; Scholes, G. D.; Mennucci, B. Electronic energy transfer in condensed phase studied by a polarizable QM/MM model. *J. Chem. Theory Comput.* **2009**, *5*, 1838–1848.

(15) Warshel, A.; Levitt, M. Theoretical Studies of Enzymic Reactions: Dielectric, Electrostatic and Steric Stabilization of the Carbonium Ion in the Reaction of Lysozyme. *J. Mol. Biol.* **1976**, *103*, 227–249.

(16) Field, M. J.; Bash, P. A.; Karplus, M. A Combined Quantum Mechanical and Molecular Mechanical Potential for Molecular Dynamics Simulations. *J. Comput. Chem.* **1990**, *11*, 700–733.

(17) Gao, J. Hybrid Quantum and Molecular Mechanical Simulations: An Alternative Avenue to Solvent Effects in Organic Chemistry. *Acc. Chem. Res.* **1996**, *29*, 298–305.

(18) Lin, H.; Truhlar, D. G. QM/MM: What Have We Learned, Where Are We, and Where Do We Go From Here? *Theor. Chem. Acc.* **2007**, *117*, 185–199.

(19) Puglisi, A.; Giovannini, T.; Antonov, L.; Cappelli, C. Interplay between conformational and solvent effects in UV-visible absorption spectra: curcumin tautomers as a case study. *Phys. Chem. Chem. Phys.* **2019**, *21*, 15504–15514.

(20) Gordon, M. S.; Smith, Q. A.; Xu, P.; Slipchenko, L. V. Accurate first principles model potentials for intermolecular interactions. *Annu. Rev. Phys. Chem.* **2013**, *64*, 553–578.

(21) DeFusco, A.; Minezawa, N.; Slipchenko, L. V.; Zahariev, F.; Gordon, M. S. Modeling solvent effects on electronic excited states. *J. Phys. Chem. Lett.* **2011**, *2*, 2184–2192.

(22) Wesolowski, T. A.; Warshel, A. Frozen density functional approach for ab initio calculations of solvated molecules. *J. Phys. Chem.* **1993**, *97*, 8050–8053.

(23) Manby, F. R.; Stella, M.; Goodpaster, J. D.; Miller III, T. F. A simple, exact density-functional-theory embedding scheme. *J. Chem. Theory Comput.* **2012**, *8*, 2564–2568.

(24) Sæther, S.; Kjærgaard, T.; Koch, H.; Høyvik, I.-M. Density-Based Multilevel Hartree–Fock Model. *J. Chem. Theory Comput.* **2017**, *13*, 5282–5290.

(25) Giovannini, T.; Koch, H. Energy-Based Molecular Orbital Localization in a Specific Spatial Region. *J. Chem. Theory Comput.* **2021**, *17*, 139–150.

(26) Marrazzini, G.; Giovannini, T.; Scavino, M.; Egidi, F.; Cappelli, C.; Koch, H. Multi-level density functional theory. *Journal of chemical theory and computation* **2021**, *17*, 791–803.

(27) Goletto, L.; Giovannini, T.; Folkestad, S. D.; Koch, H. Combining multilevel Hartree–Fock and multilevel coupled cluster approaches with molecular mechanics: a study of electronic excitations in solutions. *Physical Chemistry Chemical Physics* **2021**, *23*, 4413–4425.

(28) Giovannini, T.; Macchiagodena, M.; Ambrosetti, M.; Puglisi, A.; Lafiosca, P.; Lo Gerfo, G.; Egidi, F.; Cappelli, C. Simulating vertical excitation energies of solvated dyes: From continuum to polarizable discrete modeling. *Int. J. Quant. Chem.* **2019**, *119*, e25684.

(29) Zuehlsdorff, T. J.; Isborn, C. M. Modeling Absorption Spectra of Molecules in Solution. *Int. J. Quant. Chem.* **2019**, *119*, e25719.

(30) Zhang, K.; Ren, S.; Caricato, M. Multi-state QM/QM Extrapolation of UV/Vis Absorption Spectra with Point Charge Embedding. *J. Chem. Theory Comput.* **2020**, *16*, 4361–4372.

(31) Gómez, S.; Giovannini, T.; Cappelli, C. Absorption spectra of xanthines in aqueous solution: a computational study. *Phys. Chem. Chem. Phys.* **2020**, *22*, 5929–5941.

(32) Watanabe, H. C.; Kubař, T.; Elstner, M. Size-Consistent Multipartitioning QM/MM: A Stable and Efficient Adaptive QM/MM Method. *Journal of Chemical Theory and Computation* **2014**, *10*, 4242–4252, PMID: 26588122.

(33) Heyden, A.; Lin, H.; Truhlar, D. G. Adaptive Partitioning in Combined Quantum Mechanical and Molecular Mechanical Calculations of Potential Energy Functions for Multiscale Simulations. *The Journal of Physical Chemistry B* **2007**, *111*, 2231–2241, PMID: 17288477.

(34) Watanabe, H. C.; Cui, Q. Quantitative Analysis of QM/MM Boundary Artifacts and Correction in Adaptive QM/MM Simulations. *Journal of Chemical Theory and Computation* **2019**, *15*, 3917–3928, PMID: 31095912.

(35) Kjellgren, E. R.; Haugaard Olsen, J. M.; Kongsted, J. Importance of Accurate Structures for Quantum Chemistry Embedding Methods: Which Strategy Is Better? *J. Chem. Theory Comput.* **2018**, *14*, 4309–4319.

(36) Perera, A. S.; Thomas, J.; Poopari, M. R.; Xu, Y. The clusters-in-a-liquid approach for solvation: new insights from the conformer specific gas phase spectroscopy and vibrational optical activity spectroscopy. *Front. Chem.* **2016**, *4*, 9.

(37) Tomasi, J.; Persico, M. Molecular Interactions in Solution: An Overview of Methods Based on Continuous Distributions of the Solvent. *Chem. Rev.* **1994**, *94*, 2027–2094.

(38) Gonzalez, C.; Restrepo-Cossio, A.; Márquez, M.; Wiberg, K. B. Ab Initio Study of the Stability of the Ylide-like Intermediate Methyleneoxonium in the Reaction between Singlet Methylene and Water. *Journal of the American Chemical Society* **1996**, *118*, 5408–5411.

(39) Tomasi, J.; Mennucci, B.; Cammi, R. Quantum Mechanical Continuum Solvation Models. *Chem. Rev.* **2005**, *105*, 2999–3094.

(40) Scalmani, G.; Frisch, M. J. Continuous surface charge polarizable continuum models of solvation. I. General formalism. *J. Chem. Phys.* **2010**, *132*, 114110.

(41) Cappelli, C.; Corni, S.; Tomasi, J. Solvent Effects on trans/gauche Conformational Equilibria of Substituted Chloroethanes: a Polarizable Continuum Model Study. *The Journal of Physical Chemistry A* **2001**, *105*, 10807–10815.

(42) Cappelli, C.; Mennucci, B. Modeling the Solvation of Peptides. The Case of (s)-N-

Acetylproline Amide in Liquid Water. *The Journal of Physical Chemistry B* **2008**, *112*, 3441–3450, PMID: 18293964.

(43) Cappelli, C. Integrated QM/polarizable MM/continuum approaches to model chiroptical properties of strongly interacting solute–solvent systems. *Int. J. Quant. Chem.* **2016**, *116*, 1532–1542.

(44) Giovannini, T.; Puglisi, A.; Ambrosetti, M.; Cappelli, C. Polarizable QM/MM Approach with Fluctuating Charges and Fluctuating Dipoles: The QM/FQFμ Model. *Journal of Chemical Theory and Computation* **2019**, *15*, 2233–2245, PMID: 30875213.

(45) Giovannini, T.; Riso, R. R.; Ambrosetti, M.; Puglisi, A.; Cappelli, C. Electronic transitions for a fully polarizable qm/mm approach based on fluctuating charges and fluctuating dipoles: linear and corrected linear response regimes. *J. Chem.Phys.* **2019**, *151*, 174104.

(46) Egidi, F.; Gerfo, G. L.; Macchiagodena, M.; Cappelli, C. On the nature of charge-transfer excitations for molecules in aqueous solution: a polarizable QM/MM study. *Theoretical Chemistry Accounts* **2018**, *137*, 1–12.

(47) Egidi, F.; Giovannini, T.; Del Frate, G.; Lemler, P. M.; Vaccaro, P. H.; Cappelli, C. A combined experimental and theoretical study of optical rotatory dispersion for (R)-glycidyl methyl ether in aqueous solution. *Phys. Chem. Chem. Phys.* **2019**, *21*, 3644–3655.

(48) Mao, Y.; Shao, Y.; Dziedzic, J.; Skylaris, C.-K.; Head-Gordon, T.; Head-Gordon, M. Performance of the AMOEBA water model in the vicinity of QM solutes: A diagnosis using energy decomposition analysis. *J. Chem. Theory Comput.* **2017**, *13*, 1963–1979.

(49) Connolly, D.; Paull, B. Rapid determination of nitrate and nitrite in drinking water samples using ion-interaction liquid chromatography. *Analytica Chimica Acta* **2001**, *441*, 53–62.

(50) Manea, F.; Remes, A.; Radovan, C.; Pode, R.; Picken, S.; Schoonman, J. Simultaneous electrochemical determination of nitrate and nitrite in aqueous solution using Ag-doped zeolite-expanded graphite-epoxy electrode. *Talanta* **2010**, *83*, 66–71.

(51) Aluker, N.; Herrmann, M.; Suzdaltseva, Y. M. A Spectrophotometric Study of Nitrate and Nitrite Salts and Their Aqueous Solutions. *Optics and Spectroscopy* **2019**, *127*, 991–996.

(52) Helaleh, M. I.; Korenaga, T. Sensitive spectrophotometric determination of nitrite in human saliva and rain water and of nitrogen dioxide in the atmosphere. *Journal of AOAC International* **2001**, *84*, 53–58.

(53) APHA, APHA Standard Method 4500—NO2-. B. 1998.

(54) Tran, C. T.; Tran, H. T.; Bui, H. T.; Dang, T. Q.; Nguyen, L. Q. Determination of low level nitrate/nitrite contamination using SERS-active Ag/ITO substrates coupled to a self-designed Raman spectroscopy system. *Journal of Science: Advanced Materials and Devices* **2017**, *2*, 172 – 177.

(55) Ianoul, A.; Coleman, T.; Asher, S. A. UV resonance Raman spectroscopic detection of nitrate and nitrite in wastewater treatment processes. *Analytical Chemistry* **2002**, *74*, 1458–1461.

(56) Opländer, C.; Suschek, C. V. The Role of Photolabile Dermal Nitric Oxide Derivates in Ultraviolet Radiation (UVR)-Induced Cell Death. *International Journal of Molecular Sciences* **2013**, *14*, 191–204.

(57) Thomas, O.; Brogat, M. In *UV-Visible Spectrophotometry of Water and Wastewater (Second Edition)*, second edition ed.; Thomas, O., Burgess, C., Eds.; Elsevier, 2017; pp 379 – 517.

(58) Zuo, Y.; Deng, Y. The near-UV absorption constants for nitrite ion in aqueous solution. *Chemosphere* **1998**, *36*, 181–188.

(59) Mizuno, H.; Oosterbaan, K. J.; Menzl, G.; Smith, J.; Rizzuto, A. M.; Geissler, P. L.; Head-Gordon, M.; Saykally, R. J. Revisiting the $\pi \to \pi^*$ transition of the nitrite ion at the air/water interface: A combined experimental and theoretical study. *Chemical Physics Letters* **2020**, 137516.

(60) Friedman, H. L. On the ultraviolet absorption spectra of uninegative ions. *The Journal of Chemical Physics* **1953**, *21*, 319–322.

(61) Sidman, J. W. Electronic and Vibrational States of the Nitrite Ion. I. Electronic States1. *Journal of the American Chemical Society* **1957**, *79*, 2669–2675.

(62) Strickler, S.; Kasha, M. Solvent effects on the electronic absorption spectrum of nitrite ion. *Journal of the American Chemical Society* **1963**, *85*, 2899–2901.

(63) EPA, U. 2018 Edition of the drinking water standards and health advisories. *EPA 822-F-18-001* **2018**,

(64) Regulations, E. European Communities (Drinking Water) Regulations. *Statutory Instruments* **2014**,

(65) Gao, M.; Fang, W.; Ren, J.; Shen, A.; Hu, J. Reliable SERS detection of nitrite based on pH and laser irradiance-dependent diazotization through a convenient sampling micro-chamber. *Analyst* **2016**, *141*, 5195–5201.

(66) Jiao, L. Z.; Dong, D. M.; Zheng, W. G.; Wu, W. B.; Feng, H. K.; Shen, C. J.; Yan, H. Determination of nitrite using UV absorption spectra based on multiple linear regression. *Asian Journal of Chemistry* **2013**, *25*, 2273–2277.

(67) Hadad, C.; Florez, E.; Acelas, N.; Merino, G.; Restrepo, A. Microsolvation of small cations and anions. *Int. J. Quant. Chem.* **2019**, *119*, e25766.

(68) Wang, J.; Wolf, R. M.; Caldwell, J. W.; Kollman, P. A.; Case, D. A. Development and testing of a general amber force field. *J. Comput. Chem.* **2004**, *25*, 1157–1174.

(69) Mark, P.; Nilsson, L. Structure and Dynamics of the TIP3P, SPC, and SPC/E Water Models at 298 K. *J. Phys. Chem. A* **2001**, *105*, 9954–9960.

(70) Abrahama, M. J.; Murtola, T.; Schulz, R.; Pálla, S.; Smith, J. C.; Hess, B.; Lindahl, E. GROMACS: High Performance Molecular Simulations through Multi-Level Parallelism from Laptops to Supercomputers. *SoftwareX* **2015**, *1-2*, 19–25.

(71) Marenich, A. V.; Jerome, S. V.; Cramer, C. J.; Truhlar, D. G. Charge Model 5: An Extension of Hirshfeld Population Analysis for the Accurate Description of Molecular Interactions in Gaseous and Condensed Phases. *J. Chem. Theory Comput.* **2012**, *8*, 527–541, PMID: 26596602.

(72) Bayly, C. I.; Cieplak, P.; Cornell, W.; Kollman, P. A. A well-behaved electrostatic potential based method using charge restraints for deriving atomic charges: the RESP model. *The Journal of Physical Chemistry* **1993**, *97*, 10269–10280.

(73) Bussi, G.; Donadio, D.; Parrinello, M. Canonical sampling through velocity rescaling. *J. Chem. Phys.* **2007**, *126*, 014101.

(74) Parrinello, M.; Rahman, A. Strain fluctuations and elastic constants. *J. Chem. Phys.* **1982**, *76*, 2662–2666.

(75) Darden, T.; York, D.; Pedersen, L. Particle mesh Ewald: An Nlog(N) method for Ewald sums in large systems. *J. Chem. Phys.* **1993**, *98*, 10089–10092.

(76) Berendsen, H. J.; Van Gunsteren, W. F. Practical algorithms for dynamic simulations. *Molecular-dynamics simulation of statistical-mechanical systems* **1986**, 43–65.

(77) Brehm, M.; Kirchner, B. TRAVIS - A Free Analyzer and Visualizer for Monte Carlo

and Molecular Dynamics Trajectories. *Journal of Chemical Information and Modeling* **2011**, *51*, 2007–2023, PMID: 21761915.

(78) Brehm, M.; Thomas, M.; Gehrke, S.; Kirchner, B. TRAVIS—A free analyzer for trajectories from molecular simulation. *The Journal of Chemical Physics* **2020**, *152*, 164105.

(79) Metropolis, N.; Rosenbluth, A. W.; Rosenbluth, M. N.; Teller, A. H.; Teller, E. Equation of State Calculations by Fast Computing Machines. *The Journal of Chemical Physics* **1953**, *21*, 1087–1092.

(80) Kirkpatrick, S.; Gelatt, C. D.; Vecchi, M. P. Optimization by Simulated Annealing. *Science* **1983**, *220*, 671–680.

(81) Pérez, J.; Restrepo, A. ASCEC V02:Annealing Simulado con Energía Cuántica. 2008; Property, development, and implementation: Grupo de Química–Física Teórica, Instituto de Química, Universidad de Antioquia, Medellín, Colombia.

(82) Pérez, J. F.; Hadad, C. Z.; Restrepo, A. Structural studies of the water tetramer. *Int. J. Quant. Chem.* **2008**, *108*, 1653–1659.

(83) Pérez, J. F.; Florez, E.; Hadad, C. Z.; Fuentealba, P.; Restrepo, A. Stochastic Search of the Quantum Conformational Space of Small Lithium and Bimetallic Lithium–Sodium Clusters. *The Journal of Physical Chemistry A* **2008**, *112*, 5749–5755.

(84) Frisch, M. J.; Trucks, G. W.; Schlegel, H. B.; Scuseria, G. E.; Robb, M. A.; Cheeseman, J. R.; Scalmani, G.; Barone, V.; Petersson, G. A.; Nakatsuji, H. et al. Gaussian 16 Revision B.01. 2016; Gaussian Inc. Wallingford CT.

(85) Boys, S.; Bernardi, F. The calculation of small molecular interactions by the differences of separate total energies. Some procedures with reduced errors. *Molecular Physics* **1970**, *19*, 553–566.

(86) Riplinger, C.; Sandhoefer, B.; Hansen, A.; Neese, F. Natural triple excitations in local coupled cluster calculations with pair natural orbitals. *The Journal of Chemical Physics* **2013**, *139*, 134101.

(87) Riplinger, C.; Neese, F. An efficient and near linear scaling pair natural orbital based local coupled cluster method. *The Journal of Chemical Physics* **2013**, *138*, 034106.

(88) Neese, F. The ORCA program system. *WIREs Computational Molecular Science* **2012**, *2*, 73–78.

(89) Weinhold, F.; Landis, C. R. *Discovering Chemistry with Natural Bond Orbitals*; Wiley-VCH, Hoboken NJ, 319pp, 2012.

(90) Glendening, E. D.; Landis, C. R.; Weinhold, F. Natural bond orbital methods. *Wiley Interdiscip. Rev. Comput. Mol. Sci.* **2012**, *2*, 1–42.

(91) Weinhold, F.; Landis, C.; Glendening, E. What is NBO analysis and how is it useful? *International Reviews in Physical Chemistry* **2016**, *35*, 399–440.

(92) Bader, R. *Atoms in Molecules: A Quantum Theory*; Oxford Univ. press Oxford, 1990.

(93) Bader, R. F. W. A quantum theory of molecular structure and its applications. *Chem. Rev.* **1991**, *91*, 893–928.

(94) Bader, R. F. W. The Quantum Mechanical Basis of Conceptual Chemistry. *Monatshefte für Chemie / Chemical Monthly* **2005**, *136*, 819–854.

(95) Popelier, P. On the full topology of the Laplacian of the electron density. *Coordin. Chem. Rev.* **2000**, *197*, 169 – 189.

(96) Popelier, P. L. *Atoms in Molecules: An Introduction*; Prentice Hall, London, 2000.

(97) Grabowski, S. J. What Is the Covalency of Hydrogen Bonding? *Chem. Rev.* **2011**, *111*, 2597–2625.

(98) Rojas-Valencia, N.; Gómez, S.; Guerra, D.; Restrepo, A. A detailed look at the bonding interactions in the microsolvation of monoatomic cations. *Phys. Chem. Chem. Phys.* **2020**, *22*, 13049–13061.

(99) Gómez, S.; Ramírez-Malule, H.; Cardona-G, W.; Osorio, E.; Restrepo, A. Double-Ring Epimerization in the Biosynthesis of Clavulanic Acid. *The Journal of Physical Chemistry A* **2020**, *124*, 9413–9426, PMID: 33135896.

(100) Espinosa, E.; Alkorta, I.; Elguero, J.; Molins, E. From weak to strong interactions: A comprehensive analysis of the topological and energetic properties of the electron density distribution involving X–H$\cdots$F–Y systems. *J. Chem. Phys.* **2002**, *117*, 5529–5542.

(101) Reed, A. E.; Weinhold, F. Natural bond orbital analysis of near-Hartree–Fock water dimer. *J. Chem. Phys.* **1983**, *78*, 4066–4073.

(102) Rengifo, E.; Gómez, S.; Arce, J. C.; Weinhold, F.; Restrepo, A. The role of hyperconjugation in the unusual conformation of thymine: A natural bond orbital analysis. *Computational and Theoretical Chemistry* **2018**, *1130*, 58 – 62.

(103) Keith, T. AIMALL *(version 13.05.06)*, 2013. aima.tkgristmill. com.

(104) Glendening, E. D.; Badenhoop, J. K.; Reed, A. E.; Carpenter, J. E.; Bohmann, J. A.; Morales, C. M.; Karafiloglou, P.; Landis, C. R.; Weinhold, F. NBO 7.0. 2018; Theoretical Chemistry Institute, University of Wisconsin, Madison, WI.

(105) Rick, S. W.; Stuart, S. J.; Berne, B. J. Dynamical fluctuating charge force fields: Application to liquid water. *J. Chem. Phys.* **1994**, *101*, 6141–6156.

(106) Giovannini, T.; Lafiosca, P.; Chandramouli, B.; Barone, V.; Cappelli, C. Effective yet reliable computation of hyperfine coupling constants in solution by a QM/MM

approach: Interplay between electrostatics and non-electrostatic effects. *The Journal of Chemical Physics* **2019**, *150*, 124102.

(107) Giovannini, T.; Lafiosca, P.; Cappelli, C. A General Route to Include Pauli Repulsion and Quantum Dispersion Effects in QM/MM Approaches. *Journal of Chemical Theory and Computation* **2017**, *13*, 4854–4870, PMID: 28898079.

(108) Giovannini, T.; Ambrosetti, M.; Cappelli, C. Quantum Confinement Effects on Solvatochromic Shifts of Molecular Solutes. *The Journal of Physical Chemistry Letters* **2019**, *10*, 5823–5829, PMID: 31518133.

(109) Giovannini, T.; Macchiagodena, M.; Ambrosetti, M.; Puglisi, A.; Lafiosca, P.; Lo Gerfo, G.; Egidi, F.; Cappelli, C. Simulating vertical excitation energies of solvated dyes: From continuum to polarizable discrete modeling. *Int. J. Quant. Chem.* **2019**, *119*, e25684.

(110) Vchirawongkwin, S.; Kritayakornupong, C.; Tongraar, A.; Vchirawongkwin, V. Hydration properties determining the reactivity of nitrite in aqueous solution. *Dalton Transactions* **2014**, *43*, 12164–12174.

(111) Yadav, S.; Chandra, A. Solvation Shell of the Nitrite Ion in Water: An Ab Initio Molecular Dynamics Study. *The Journal of Physical Chemistry B* **2020**, *124*, 7194–7204.

(112) Lee, N.; Keesee, R.; Castleman Jr, A. On the correlation of total and partial enthalpies of ion solvation and the relationship to the energy barrier to nucleation. *Journal of Colloid and Interface Science* **1980**, *75*, 555–565.

(113) Flórez, E.; Acelas, N.; Ibargüen, C.; Mondal, S.; Cabellos, J. L.; Merino, G.; Restrepo, A. Microsolvation of NO_3^-: structural exploration and bonding analysis. *RSC Adv.* **2016**, *6*, 71913–71923.

(114) Acelas, N.; Flórez, E.; Hadad, C.; Merino, G.; Restrepo, A. A Comprehensive Picture of the Structures, Energies, and Bonding in $[SO_4(H_2O)_n]^{2-}$, n = 1–6. *J. Phys. Chem. A* **2019**, *123*, 8650–8656.

(115) David, J.; Guerra, D.; Restrepo, A. Structural characterization of the (methanol) 4 potential energy surface. *The Journal of Physical Chemistry A* **2009**, *113*, 10167–10173.

(116) Murillo, J.; David, J.; Restrepo, A. Insights into the structure and stability of the carbonic acid dimer. *Physical Chemistry Chemical Physics* **2010**, *12*, 10963–10970.

(117) Romero, J.; Reyes, A.; David, J.; Restrepo, A. Understanding microsolvation of Li+: structural and energetical analyses. *Phys. Chem. Chem. Phys.* **2011**, *13*, 15264–15271.

(118) Gonzalez, J. D.; Florez, E.; Romero, J.; Reyes, A.; Restrepo, A. Microsolvation of Mg^{2+}, Ca^{2+}: strong influence of formal charges in hydrogen bond networks. *J. Mol. Model.* **2013**, *19*, 1763–1777.

(119) Zapata-Escobar, A.; Manrique-Moreno, M.; Guerra, D.; Hadad, C. Z.; Restrepo, A. A combined experimental and computational study of the molecular interactions between anionic ibuprofen and water. *J. Chem. Phys.* **2014**, *140*, 184312.

(120) Ibargüen, C.; Manrique-Moreno, M.; Hadad, C. Z.; David, J.; Restrepo, A. Microsolvation of dimethylphosphate: a molecular model for the interaction of cell membranes with water. *Phys. Chem. Chem. Phys.* **2013**, *15*, 3203–3211.

(121) Rojas-Valencia, N.; Ibargüen, C.; Restrepo, A. Molecular interactions in the microsolvation of dimethylphosphate. *Chem. Phys. Lett.* **2015**, *635*, 301 – 305.

(122) Flórez, E.; Acelas, N.; Ramírez, F.; Hadad, C.; Restrepo, A. Microsolvation of F^-. *Phys. Chem. Chem. Phys.* **2018**, *20*, 8909–8916.

(123) Vargas-Caamal, A.; Cabellos, J. L.; Ortiz-Chi, F.; Rzepa, H. S.; Restrepo, A.; Merino, G. How Many Water Molecules Does it Take to Dissociate HCl? *Chemistry – A European Journal* **2016**, *22*, 2812–2818.

(124) Flórez, E.; Maldonado, A. F.; Aucar, G. A.; David, J.; Restrepo, A. Microsolvation of methylmercury: structures, energies, bonding and NMR constants (199Hg, 13C and 17O). *Phys. Chem. Chem. Phys.* **2016**, *18*, 1537–1550.

(125) Chamorro, Y.; Flórez, E.; Maldonado, A.; Aucar, G.; Restrepo, A. Microsolvation of heavy halides. *International Journal of Quantum Chemistry* **2021**, *121*, e26571.

(126) Ramírez-Rodríguez, F.; Restrepo, A. Structures, energies, and bonding in the microsolvation of Na+. *Chemical Physics* **2021**, 111106.

(127) Ramírez, F.; Hadad, C.; Guerra, D.; David, J.; Restrepo, A. Structural studies of the water pentamer. *Chem. Phys. Lett.* **2011**, *507*, 229 – 233.

(128) Hincapié, G.; Acelas, N.; Castaño, M.; David, J.; Restrepo, A. Structural Studies of the Water Hexamer. *J. Phys. Chem. A* **2010**, *114*, 7809–7814.

(129) Acelas, N.; Hincapié, G.; Guerra, D.; David, J.; Restrepo, A. Structures, energies, and bonding in the water heptamer. *J. Chem. Phys.* **2013**, *139*, 044310.

(130) Lalitha, M.; Senthilkumar, L. DFT study on $X^-(H_2O)(n= 1-10)(X=OH, NO_2, NO_3, CO_3)$ anionic water cluster. *Journal of molecular graphics & modelling* **2014**, *54*, 148.

(131) Pathak, A. K.; Mukherjee, T.; Maity, D. K. Microhydration of NO3-: A Theoretical Study on Structure, Stability and IR Spectra. *The Journal of Physical Chemistry A* **2008**, *112*, 3399–3408, PMID: 18327926.

(132) Giovannini, T.; Ambrosetti, M.; Cappelli, C. Quantum confinement effects on solvatochromic shifts of molecular solutes. *J. Phys. Chem. Lett.* **2019**, *10*, 5823–5829.

(133) Smith, J. W.; Lam, R. K.; Shih, O.; Rizzuto, A. M.; Prendergast, D.; Saykally, R. J. Properties of aqueous nitrate and nitrite from x-ray absorption spectroscopy. *The Journal of chemical physics* **2015**, *143*, 084503.